

# Improved accuracy and robustness of electron density profiles from JET's X-mode Frequency-Modulated Continuous-Wave reflectometers

R. B. Morales,<sup>1</sup> A. Salmi,<sup>2</sup> P. Abreu,<sup>3</sup> C. H. S. Amador,<sup>4</sup> L. Appel,<sup>1</sup> P. Carman,<sup>1</sup> J. Fessey,<sup>1</sup> J. Flanagan,<sup>1</sup> M. Fontana,<sup>1</sup> L. Frassinetti,<sup>5</sup> C. Giroud,<sup>1</sup> S. Hacquin,<sup>6</sup> S. Heurax,<sup>7</sup> L. Meneses,<sup>8</sup> G. Ronchi,<sup>9</sup> R. Sabot,<sup>6</sup> A. Silva,<sup>3</sup> A. Sirinelli,<sup>8</sup> G. Szepesi,<sup>1</sup> D. Taylor,<sup>1</sup> and D. Terranova<sup>10</sup>

<sup>1</sup>UKAEA, Culham Science Centre, Abingdon, Oxfordshire, OX14 3DB, United Kingdom

<sup>2</sup>VTT, P.O. Box 1000, FI-02044 VTT, Espoo, Finland

<sup>3</sup>IPFN, Instituto Superior Técnico da Universidade de Lisboa, 1049-001 Lisboa, Portugal

<sup>4</sup>Federal University of Technology - Parana (UTFPR), Department of Natural Sciences, Cornélio Procópio, Brazil

<sup>5</sup>Division of Electromagnetic Engineering and Fusion Science, KTH, Stockholm, 100 44, Sweden

<sup>6</sup>IRFM, CEA Cadarache, 13108 Saint-Paul-lez-Durance, France

<sup>7</sup>IJL, University of Lorraine, UMR 7198 CNRS, BP 50840, 54011 Nancy Cedex, France

<sup>8</sup>ITER Organization, Route de Vinon, CS 90 046, 13067 Saint-Paul-Lez-Durance, France

<sup>9</sup>Oak Ridge National Laboratory, Oak Ridge, Tennessee, TN 37830, USA

<sup>10</sup>Consorzio RFX and ISTP-CNR, Corso Stati Uniti 4 - 35127 Padova, Italy

(\*Electronic mail: Rennan.BMorales@ukaea.uk)

(Dated: 23 February 2024)

JET's frequency-modulated continuous wave (FMCW) reflectometers have been operating well with the current design since 2005 and density profiles have been automatically calculated intershot since then. However, the calculated profiles had long suffered from several shortcomings: poor agreement with other diagnostics; sometimes inappropriately moving radially by several centimeters; elevated level of radial jitter; and persistent wiggles (strong unphysical oscillations). In this research, several techniques are applied to the reflectometry data analysis and the shortcomings are significantly improved. Starting with improving the equilibrium reconstruction that estimates the background magnetic field, also adding a ripple correction in the reconstructed magnetic field profile, and new inner-wall reflection positions estimated through ray-tracing, these changes not only improve the agreement of reconstructed profiles to other diagnostics but also solve density profile wiggles that were present during band transitions. Other smaller but also persistent wiggles were also suppressed by applying a localized correction to the measured beat frequency where persistent oscillations are present. Lastly, the burst analysis method, as introduced in [P. Varela et al 2006 Nucl. Fusion 46 S693], has been implemented to extract the beat frequency from stacked spectrograms. Due to the strong suppression of spurious reflections, the radial jitter that sometimes would span several centimeters has been strongly reduced. The stacking of spectrograms has also been shown to be very useful for stacking recurring events, like small gas puff modulations, and extracting transport coefficients that would otherwise be below the noise level.

## I. INTRODUCTION

JET's frequency-modulated continuous-wave (FMCW) reflectometers have been operating well with the current design since 2005 and density profiles are being automatically calculated intershot since then<sup>1-3</sup>. The standard profiles automatically produced are reconstructed from the instantaneous phase increment from the X-mode bands Q, V, W and D, depending on the background magnetic field, swept over the full probing frequency range (42-145.8 GHz) in 12  $\mu$ s, with the fastest possible repetition rate of one sweep every 15  $\mu$ s and a maximum of 100.000 profiles per pulse, as per the acquisition memory limitation. Apart from adjusting trigger timings, the diagnostic operates automatically and the intershot profile reconstruction code always provides electron density profiles as long as the on-axis magnetic field is at least 1.9 T. Nevertheless, the calculated profiles had long suffered from several shortcomings: poor agreement to other diagnostics; sometimes inappropriately moving radially by several centimeters; elevated level of radial jitter; and persistent wiggles (strong unphysical oscillations in the reconstructed density profiles),

sometimes associated, but not exclusive, to band junctions. In this research, several techniques are applied in the reflectometry data analysis and the shortcomings are significantly improved. All improvements are demonstrated via example profiles and absolute position benchmarks, with all enhancements together benchmarked at the end of this contribution with an example application.

All optimized variables that impact the quality of the reconstructed density profiles are connected to the recursive profile reconstruction formula that can be written as

$$R_n = R_{n-1} + \frac{1}{W} \frac{\Delta\phi_{pla}(f_{prob}^n)}{N_{R_{n-1}}(f_{prob}^n, f_{pe}, f_{ce})}, \quad (1)$$

with  $R_n$  being the next cut-off position to be calculated,  $R_{n-1}$  the previous already calculated cut-off position,  $W$  the weight factor which is typically a constant  $2/3^{4,5}$ , but can be optimized to match the shape of the refractive index<sup>6</sup>,  $N_{R_{n-1}}(f_{prob}^n, f_{pe}, f_{ce})$  the refractive index for probing frequency  $f_{prob}^n$  at position  $R_{n-1}$  and  $\Delta\phi_{pla}$  being the phase increment from propagation along the plasma due to a probing

frequency step  $f_{prob}^{n-1}$  to  $f_{prob}^n$ , which is computed as

$$\Delta\varphi_{pla}(f_{prob}^n) = \Delta\varphi_{meas}(f_{prob}^n) - \Delta\varphi_{ref}(f_{prob}^n) + \Delta\varphi_{vac}(f_{prob}^n), \quad (2)$$

where  $\Delta\varphi_{meas}(f_{prob}^n)$  is the total phase increment measured,  $\Delta\varphi_{ref}(f_{prob}^n)$  the reference vacuum phase increment measured before plasma and  $\Delta\varphi_{vac}(f_{prob}^n)$  the excess subtracted vacuum propagation phase increment within  $\Delta\varphi_{ref}(f_{prob}^n)$  that needs to be added back numerically as calculated by

$$\Delta\varphi_{vac}(f_{prob}^n) = \frac{4\pi(f_{prob}^n - f_{prob}^{n-1})}{c}(R_{wall} - R_0), \quad (3)$$

with  $R_{wall}$  being the position at which the probing beam is reflected at the inner wall during the reference measurement,  $c$  the speed of light in vacuum, and  $R_0$  the initial profile reconstruction position (also known as initialization position). The value of  $R_0$  is determined by first finding the first probing frequency with signal amplitude above a threshold in the amplitude ramp during the transparent to opaque transition. See full method description in the reference<sup>7</sup>. From the determined  $f_{prob}^0$ , the corresponding radial position, i.e.  $R_0$ , is found in the equilibrium  $f_{ce}$  profile, since the upper X-mode cut-off converges to  $f_{ce}$  when the electron density goes to zero.

The other phase increments on the right-hand side of Eq. 2 are extracted either by taking the argument of the reflectometer signal (called the instantaneous phase), i.e. the argument of  $S(t) = A(t)\cos[\varphi(t)]$ , with  $A(t)$  being the amplitude in time, or via the beat frequency ( $f_{beat}$ ) extracted from the maximum of a spectrogram of the reflectometer signal, since the beat frequency is related to the phase through:

$$f_{beat}(t) = \frac{1}{2\pi} \frac{\partial\varphi}{\partial t} = \frac{\partial\varphi}{\partial f_{prob}} \frac{\partial f_{prob}}{\partial t} = \tau_g(f_{prob}) \cdot V_s, \quad (4)$$

where  $\tau_g$  is the group delay,  $V_s$  the sweeping rate of the probing frequency, and the phase term,  $\varphi$ , refers to the measurement phase increment  $\varphi_{ref}$  and  $\varphi_{meas}$  in Eq. 2, depending on if the measurement is performed before or after plasma breakdown, respectively.

Isolating  $\tau_g$  and integrating over  $f_{prob}$  leads to the expression used to compute the phase from the extracted beat frequency:

$$\varphi(f_{prob}) = \int f_{beat}(f_{prob})/V_s df_{prob}. \quad (5)$$

The absolute position of the reconstructed profiles is benchmarked by comparing the density profile's pedestal position of the HRTS (High-Resolution Thompson Scattering) diagnostic to the FM-CW reflectometry diagnostic, following the methodology described in Sec. II. Even though it's common to compare the reflectometry profiles to the data from other diagnostics, the benchmarking of the absolute position from numerous pulses across an experimental campaign is novel in this contribution. The theoretically achievable precision

of reflectometry reconstructed profiles can be calculated in terms of the experimental signal-to-noise ratio<sup>8</sup> or turbulence level<sup>9</sup>, but in practice, there are many aspects in calibrations and data analysis that end up adding to the final error of the reconstructed profiles. The benchmarks in this contribution highlight the final accuracy achieved experimentally for randomly selected flat-top plasmas along an experimental campaign when running an automatic profile reconstruction algorithm. Furthermore, these benchmarks were crucial to expose systematic errors and to observe how accurate the measurements are in practice for a wide range of plasma conditions.

The first benchmark of reconstructed profiles position done in Sec. V uses profiles automatically reconstructed intershot with the instantaneous phase increment, while the final benchmark in Sec. X, when the burst technique is implemented, uses the phase increment from the beat frequency of stacked spectrograms.

First and foremost, X-mode profiles can only be as radially accurate as the magnetic field profile provided from the equilibrium reconstruction. This is because the reconstructed cut-off profile is anchored to the  $f_{ce}$  profile at the initialization step (determination of  $R_0$ ). Eq. 3 shows how the  $R_0$  is used in the calculation of the phase increment for every probing frequency step, and therefore every reconstructed cut-off position from Eq. 1, as demonstrated in Chap. 5 of reference<sup>10</sup>. For reference, the initialization technique implemented in the intershot analysis using the instantaneous phase increment is based on an amplitude rise threshold<sup>7</sup>. When running the burst analysis that uses the phase increment from the beat frequency of stacked spectrograms, the same technique is implemented with the only difference that the amplitude signals are averaged over the burst. The advances in the equilibrium reconstruction in JET that provide the  $f_{ce}$  profile input are discussed in Sec. III. The enhanced equilibrium has a new pressure constraint from the HRTS data and intershot NBI fast ion deposition modeling. Even though constraining an input pressure is already shown, see references to equilibrium codes LIUQE<sup>11</sup> and CLISTE<sup>12</sup>, an extensive optimization of the data analyses and calibration was also done in JET<sup>13</sup>, with another improvement on the equilibrium access library specifically affecting the reflectometry profiles first reported here.

Eq. 3 also shows a contribution from  $R_{wall}$ , the inner-wall reflection position. This contribution refers to the pre-plasma measurement that corrects for the dispersion across the whole system ( $\Delta\varphi_{ref}$  in Eq. 2). In comparison, most experiments can afford to have a mobile system due to lower restrictions against radiation interference and access boundaries, and the dispersion is measured on a testing bench using a metallic reflecting plate, as reported e.g. in JT-60<sup>14</sup>, EAST<sup>15</sup> and W7-AS<sup>16</sup>, the latter also with in-vessel wall measurement during campaigns. At Tore Supra, a direct emission to reception antenna coupling was used for the reference phase measurement<sup>17,18</sup>. A less mobile system, closer to the JET set-up, was installed at DIII-D and the dispersion measurements are performed with the injected beam being reflected at a dedicated closed shutter at the vessel port<sup>19-21</sup>. Another alternative for JET would be to use an in-vessel mirror with a well-known location instead of the inner wall. Installing

an in-vessel mirror is a rather complex task at JET that not only needs scarce in-vessel access but also must be performed via remote handling. Furthermore, any secondary reflections from the mirror structure can degrade the measurement and further adaptations and iterations could be necessary to improve the signal quality. Since the inner wall signals are strong enough and used with reasonable success (especially after the corrections described in Sec. IV), the reference measurement used is always taken from the inner-wall pre-plasma measurement. Due to the intricate topology in that region, ray-tracing calculations were performed to reveal the location where the probing waves that are detected are being reflected, a measure realized for the first time to optimize the extraction of a system's dispersion when the probing waves are reflected at the vessel's inner-wall. The resulting reflection positions and impact on reconstructed profiles are reported in Sec. IV.

Benchmarking the reconstructed profiles' absolute position with the new inner-wall reflection positions and upgraded equilibrium revealed higher discrepancies in low background magnetic fields when the Q-band was used to measure the plasma edge. This low-field discrepancy has been eliminated with the implementation of two improvements. First, the sweep-time parameter is set with higher precision and saved more accurately without rounding or truncation. Secondly, the fit of the vacuum reference signal ( $\Delta\phi_{ref}(f_n)$  in Eq. 2) has been optimized by pre-applying a narrower band-pass filter. These optimizations are discussed in Sec. VI.

Because the injected waves start being reflected at very low densities, resulting in initialization of the profile reconstruction (determination of  $R_0$  in Eq. 3) very close to the vessel outer wall, the initialization step (anchoring  $R_0$  to  $f_{ce}$ ) has a discrepancy associated to the  $f_{ce}$  profile from the equilibrium reconstruction having a small error due to the ripple effect. The calculation of the magnitude of the ripple effect has been well-known for a long time<sup>22</sup> and JET even had a campaign dedicated to investigating the impact on the plasma performance due to the ripple effect<sup>23</sup>. Nevertheless, the ripple magnitude in JET has not been quantified specifically for the reflectometry line-of-sight before and it has been performed in this contribution as described in Sec. VII.

All improvements discussed above address the absolute radial position of the reconstructed profiles, but they still suffer from strong radial jitter due to spurious reflections and edge turbulence, and localized radial oscillations (zig-zags). The former has been improved with the implementation of the burst mode analysis described in Sec. VIII, equivalent to the method described in the original reference<sup>24</sup> and the latter with oscillation-reducing calibrations developed in this contribution for the first time, as discussed in Sec. IX. Another radial position benchmark after all aforementioned improvements is presented in Sec. X, followed by an example application of the improved profiles to the ELM cycle in Sec. XI and conclusions and prospects in Sec. XII.

## II. METHODOLOGY FOR BENCHMARKING THE ABSOLUTE POSITION OF RECONSTRUCTED PROFILES

In order to observe changes in absolute radial positions of the reflectometry profiles, the pedestal positions of the reflectometry profiles are compared to the equivalent pedestal positions from the HRTS (High Resolution Thompson Scattering) profiles, where both profiles are projected to the midplane. The HRTS diagnostic is located at the low field side, also very close to the midplane. Thus, changes from projecting the data to the midplane are small, and the respective possible errors due to performing the projections are also small. The HRTS diagnostic has a good radial position consistency along one calibration dataset and provides a good reference to observe the consistency of the absolute location of reconstructed profiles from the reflectometry data. Thus, all comparisons in this contribution include discharges from a single HRTS calibration window, which in this case corresponds to the JET's C38 deuterium campaign in 2019, with pulse range 93223 to 96563.

The pedestal position in this contribution is calculated using a simple model for higher robustness and availability. The pedestal top is assumed to be at the normalized square root of poloidal flux,  $\rho$ , equal to 0.85 and the pedestal position to be at the location corresponding to half of the density of the pedestal top. Due to a higher consistency and availability in HRTS profiles compared to the reflectometry profiles, the pedestal position and density are first calculated for the HRTS data. Next, the corresponding pedestal density is found in the reflectometry profile and its location is the reflectometry pedestal position. An example of this methodology and obtained parameters can be seen in Fig. 1. Due to the flatness of the pedestal top and the steepness of the pedestal, the method is insensitive to small variations of the defined pedestal top (and pedestal density). This was verified by changing the defined pedestal top location from  $\rho=0.85$  to either  $\rho=0.9$  or  $\rho=0.8$  and observing the impact on the calculated gaps between HRTS and reflectometry profiles ( $R_{ped}(HRTS) - R_{ped}(Ref.)$ ), both projected to the midplane). The gap values are practically identical regardless of the choice of the pedestal top location. Even though not the most precise method to estimate the pedestal position, the parameter of interest in this study is not the pedestal position itself but the consistent gap in absolute profile position between reflectometry and HRTS profiles. Therefore, since the absolute position discrepancies manifest as entire profile shifts, the extraction of the gap parameter is not sensitive to the accuracy of the estimated pedestal position. This method is very robust and adequate to demonstrate trends in datasets that reveal the overall consistency of the absolute position of the reflectometry profiles. Therefore, it is employed in this contribution whenever the absolute position of reflectometry profiles is benchmarked.

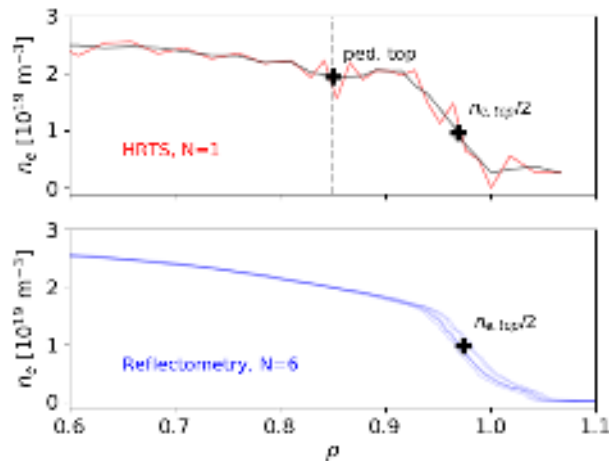


FIG. 1. Example of pedestal top density (extracted at  $\rho=0.85$ ) and position at half the top density ( $n_{e,top}/2$ ) extracted from HRTS (High Resolution Thomson Scattering), followed by the pedestal position at the same density calculated from the reflectometry profiles, from JET's pulse 93620 showing the profiles during 0.05 s from  $t=11.65$  s. The fluctuations in the HRTS profile are suppressed by lightly smoothing the profile as shown in the black curve.  $N$  indicates the number of profiles plotted from the investigated time window.

### III. PROGRESS IN EQUILIBRIUM RECONSTRUCTION

Since the beginning of the reflectometers operation at JET, a large discrepancy has been observed in the expected radial location of the reconstructed density profiles. Because the magnetic field profile from the equilibrium reconstruction also suffered from strong imprecisions (initially mostly at the toroidal field component), the location of reflectometer profiles was being adjusted with a correction factor on the input toroidal magnetic field. This correction was routinely performed as a validation step for the reflectometry profiles. The installation of an LKCO system (High Accuracy Bi-directional DC AC Fiber Optic Current Measurement) has enabled much more accurate toroidal field measurements (routinely from JET pulse 92505, at the end of 2017), but the reflectometry profiles still suffered from unexpected radial movements that were emphasized during plasma current ramps. The unexpected radial movements were solved with an update of the equilibrium access library. As part of a standard overhaul work to the equilibrium access library, a bug that exclusively affected the reflectometry data processing was discovered and fixed. The problem was an unnecessary flux renormalization step in reading back the library's generated file format. The improved stability in the reconstructed profiles can be observed in Fig. 2.

Even after the overhaul of the equilibrium access library and the new LKCO system operating routinely from JET pulse 92505, the LCFS (Last Closed Flux-Surface) position provided by the equilibrium reconstruction still showed a large disagreement with its expected position of matching the 100 eV from the temperature profile<sup>25</sup> measured with the HRTS,

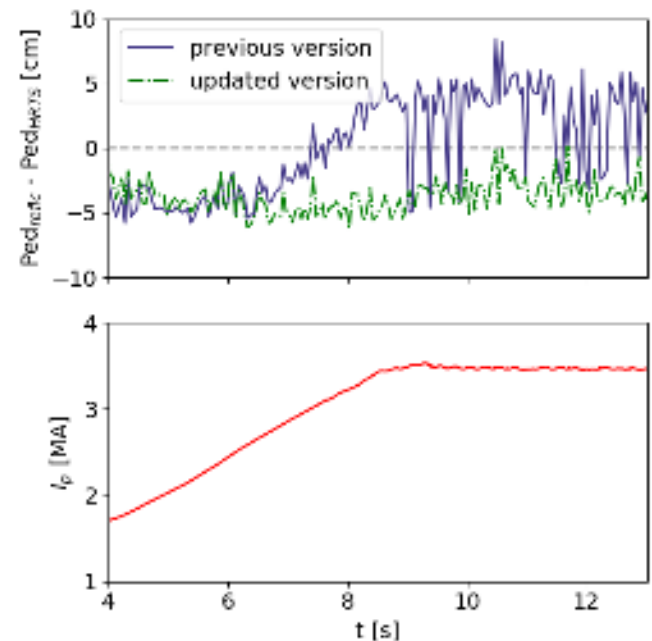


FIG. 2. Improved position of reconstructed profiles with the update of the equilibrium access library, from version 2.0.7 to 2.2.2, along a plasma current ramp in JET pulse 92437. The pedestal position tracking uses the methodology explained in Sec. II and only takes the reflectometry profiles closest to the HRTS triggers for comparison.

see Fig. 3 for the former equilibrium reconstruction technique in orange. The agreement is rather spread between 0.5 and 6 cm, with the shifting clusters corresponding to different experimental campaigns. Several enhancements in the equilibrium reconstruction technique led to an overhauled equilibrium, as plotted in blue, which resulted in a much lower campaign-to-campaign variation and campaign averages between  $\pm 1$  cm. These enhancements included an automated magnetic sensor selection method to utilize all available signals avoiding faulty measurements (previously the selection was hard coded and limited to significantly fewer sensors), a review of the calibration factors on some of the magnetic sensors, and adding a pressure constraint in the equilibrium reconstruction to account for the diamagnetic effect<sup>13</sup>. The input pressure comes from HRTS data and intershot NBI fast ion deposition modeling (when available). The improved equilibrium has been validated by checking its consistency against Thomson scattering data on a large database, by comparing the computed strike point positions against IR camera images, and by checking the symmetry of ECE profiles around the magnetic axis. The details of the validation are presented in the reference<sup>13</sup>. The equilibrium reconstruction accounts for both the calculation of the poloidal magnetic field as well as the diamagnetic correction of the toroidal field. The ripple effect is an additional new variable introduced in this contribution that applies specifically to the reflectometers' line-of-sight and is discussed later in Sec. VII.

All the improvements in the input magnetic field resulted

in more stable profile positions and better agreement between all diagnostics, and specifically to this contribution, between reflectometry, interferometry, HRTS and Li-beam.

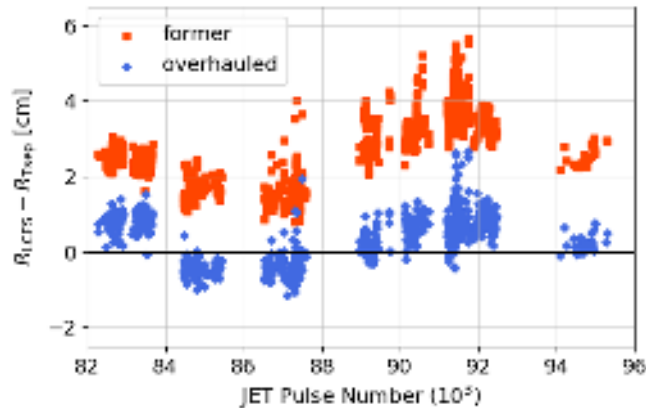


FIG. 3. Comparison of LCFS position ( $R_{LCFS}$ ) from the equilibrium reconstruction to the 100 eV location in the HRTS electron temperature profile ( $R_{T,sep}$ ) between the former equilibrium code and the overhauled equilibrium.

This enhanced profile position stability allowed to eliminate the manual adjustment of the input toroidal magnetic field since it can possibly add unphysical time-dependent effects on the reflectometry profiles. Therefore, all reconstructed profiles and respective pedestal positions discussed across this entire contribution never had any manual adjustments on the input magnetic field profile to radially move the reconstructed profiles. Further improvements, as elaborated below, are related to the reflectometry data and profile reconstruction techniques.

#### IV. INNER-WALL REFLECTION POSITIONS

The propagation path length during a pre-plasma measurement has been re-assessed due to the complex structure directly across the reflectometry injection and reception points making the exact reflection location (and respective propagation path) unclear. The exact inner-wall reflection positions need to be determined because it affects the profile reconstruction at each radial step via the  $R_{wall}$  parameter in Eq. 3. Fig. 4 shows the waveguides layout at the injection location from JET's CAD drawings. The profile reflectometers use the bottom row of open waveguides. The center waveguide is used as reception for all frequency bands, while the two side waveguides inject alternating frequency bands.

On the inner-wall side, Fig. 5 shows the location opposite to the reflectometry waveguides. From the left emission waveguide, the center of the probing beam (as illustrated by the left pink arrow) is reflected at the inner wall guard. The center of the beam from the right emission waveguide (right pink arrow), on the other hand, is reflected at the limiter (green curved structure).

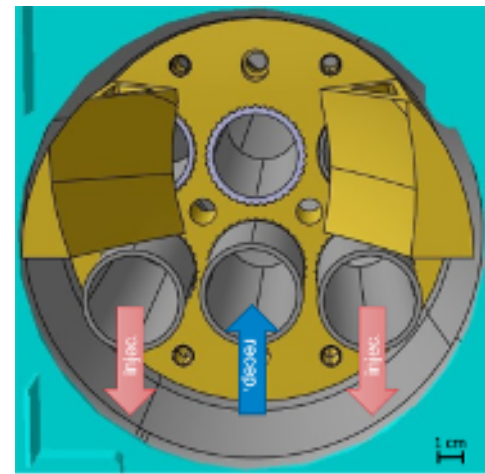


FIG. 4. CAD drawings of injection and reception waveguides used by JET's profile reflectometers.

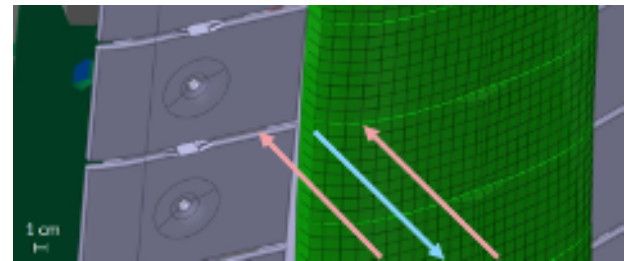


FIG. 5. Detailed structure at the inner wall of JET just opposite the reflectometry waveguides. The pink arrows show the wall positions just opposite the injection waveguides, while the blue arrow shows the inner wall position just opposite the reception waveguide. The gray structures are wall guard tiles, while the green structure is a limiter.

The automatic profile reconstruction algorithm initially assumed that the detected beams were being reflected at the rear inner-wall guard tile or a blend between the tile and the limiter, equivalent to the gray area on the toroidal cross-section depicted in Fig. 6. Following this reasoning, the respective inner-wall reflection position was taken as  $R_{wall} = 1.78m$ .

Ray-tracing calculations were performed to determine the exact reflection position at the inner wall. Fig. 7 shows beams reflected at the guard tile and limiter just opposite the reception waveguide, for the right injection waveguide in (a) and the left injection waveguide in (b). The red beam impinges on the limiter, while the blue beam on the guard tile. As seen, the beam section impinging in this area does not return to the reception waveguide. For a zoomed view of the tiles to limiter transition and validation of these ray-tracing calculations, refer to Appendix A.

As the injected beam is reflected further towards the limiter center (higher  $y$  coordinate in Figs. 5 to 8), the limiter flattens (as can be seen clearer in Figs. 5 and 34) and the impinging rays eventually reach the reception waveguide, as shown by Fig. 8. The detectable part of the beam can only be reflected at the limiter section illuminated by the green cone because in

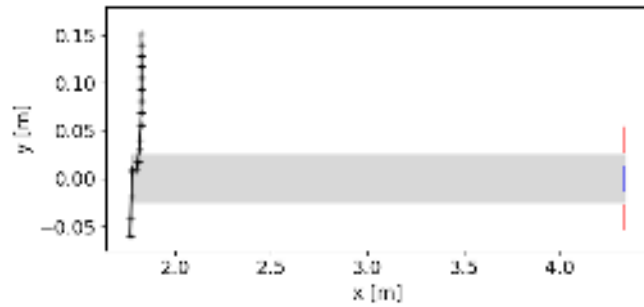


FIG. 6. Toroidal cross-section representing the reflectometry injection waveguides on the right, with the injection waveguides (top and bottom) in red and the reception waveguide (center) in blue, and the tiles and limiter at the inner wall depicted on the left. The gray area illustrates the initial location where the detected beam was expected to be coming from.

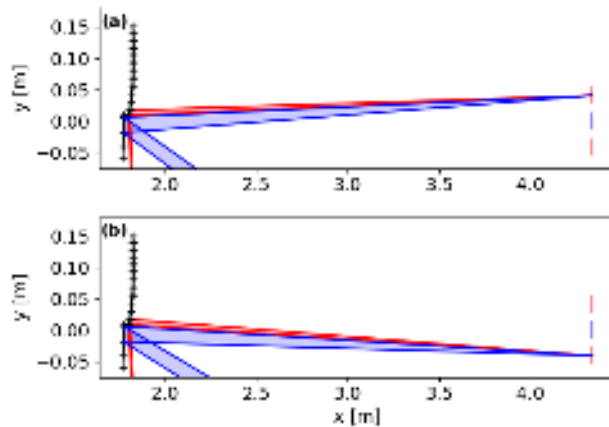


FIG. 7. Ray-tracing of beams from the right waveguide (a) and left waveguide (b), being reflected just opposite the reception waveguide at the guard tile (blue beam) and limiter (red beam). Calculated on a vacuum media since the reference measurement is performed before plasma breakdown.

Fig. 8 outside of this cone the reflected beam does not reach the reception waveguide. Since the limiter section illuminated by the green cone is rather small, it can already be used as the reflection location and it's not necessary to restrict the section further to pinpoint the exact area that illuminates the reception waveguide. Any further refinement would certainly be smaller than the experimental accuracy in the input coordinates and knowledge of the limiter surface.

The ray-tracing calculations shown in Fig. 8 illustrate how the injected waves are being reflected further out into the limiter (closer to the center of the limiter) instead of just opposite to the injection points. It also shows how much the probing beam diverges when propagating the whole distance to the inner wall and back, which corroborates the experimental observation of much reduced detected power compared to when the probing waves reflect at the plasma much closer to the waveguides. Lastly, since the probing waves are injected from two

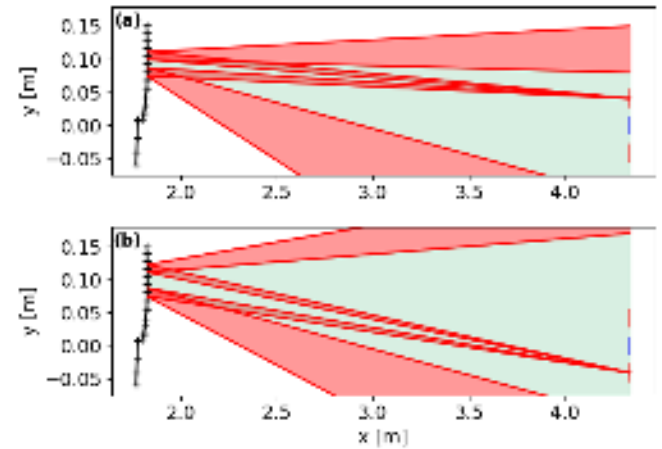


FIG. 8. Ray-tracing of waves injected from the right (a) and left (b) waveguides impinging closer to the center of the limiter structure. In blue is the center reception waveguide, which can only receive probing waves injected inside the green cone. Calculated on a vacuum media since the reference measurement is performed before plasma breakdown.

open waveguides, each probing band has been assigned a separate path length associated with the respective waveguide it goes through.

The vertical angle of incidence in the limiter is also not perfectly  $90^\circ$ , but  $88.87^\circ$ . Therefore, the center of the detected line-of-sight is higher, by 4.5 cm, causing an additional tiny 0.5 mm correction on the trajectory length (see Fig. 9).

Overall, the radial inner-wall position changed from the initial wall guard at 1.78 m to 1.8285 m for the frequency bands going through the left waveguide and 1.833 m for the frequency bands going through the right waveguide. These are not the exact limiter positions but the values that give the equivalent path length considering a straight propagation to simplify the calculation of Eq. 3.

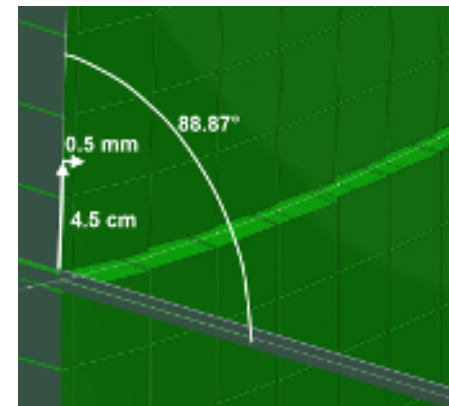


FIG. 9. Vertical angle of incidence at the inner-wall limiter directly across the injected probing microwaves.

An example of the impact on the reconstructed profiles can be observed in Fig. 10 by comparing a profile in red, recon-

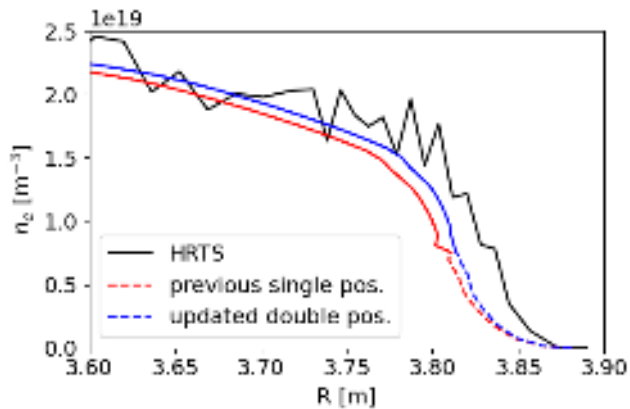


FIG. 10. Example profiles showing the typical difference between the profiles calculated using the previous single inner wall position to the profiles calculated using the updated double positions from ray-tracing. The dashed lines used data from the V probing band, while the solid lines used data from the W probing band. Reflectometry profiles are averaged from 8 profiles of consecutive triggers around a single HRTS trigger. The reflectometry profile reconstructions used the latest equilibrium and access library routine together with the updated inner-wall positions, but no other improvements that are discussed over the next sections. JET pulse 93620,  $t=12.02$  s.

structured with the initial reflection position at the wall guard, to the profile in blue reconstructed with the updated double positions. The scrape-off layer profiles don't change significantly for two reasons. First, because the initialization technique fixes the start of the density profiles to the  $f_{ce}$  profiles, thus not being affected by a  $\Delta\phi_{vac}$  contribution. Secondly, because at the low cut-off gradient along the scrape-off layer, the group delay is higher than at a high cut-off gradient along the pedestal, as can be observed in the example group delay signal of Fig. 24. The higher group delay at the scrape-off layer is due to a longer propagation close to the cut-off frequency, thus at a much lower group velocity. Therefore, at the scrape-off layer, the contribution of  $\Delta\phi_{vac}$  in  $\Delta\phi_{pla}$  (given by Eq. 2) is small compared to  $\Delta\phi_{meas}$  and  $\Delta\phi_{ref}$ . As the reconstruction gets to the pedestal, the group delay drops, and the percentile contribution of  $\Delta\phi_{vac}$  becomes more significant in  $\Delta\phi_{pla}$ , thus affecting more the reconstruction radial step as computed via Eq. 1. For the example given in Fig. 10, the total radial shift accumulated through the pedestal is an outward shift of  $\approx 1.5$  cm when using the updated inner-wall positions, thus improving the agreement to the HRTS profiles. As the profile reconstruction goes over the pedestal, the cut-off gradient drops again and the group delay increases (can be observed in the example signals shown in Figs. 21 to 23) the group delay increases again, and the relative contribution of  $\Delta\phi_{vac}$  decreases accordingly, decreasing more and more the impact on the computed radial steps. The shift accumulated over the pedestal stays practically the same all the way into the plasma core. Lastly, as can be seen in the pedestal region, around  $R=3.8$  m, there is an oscillation during a band transition, which is eliminated when using the updated band-

dependent inner-wall positions.

These results show the importance of knowing well the reflection positions if the system dispersion measurements are being done or planned at the inner wall. The development of future systems can consider these results and access the inner wall topology to develop an informed strategy for the dispersion measurements.

## V. BENCHMARK OF THE ABSOLUTE POSITION OF REFLECTOMETRY PROFILES

Initially, the reflectometry density profiles had poor consistency in their absolute position and sometimes had large discrepancies compared to other diagnostics. Significant improvements were achieved in consistency with the overhauled equilibrium access routine, as shown in Fig. 2, and the improved equilibrium reconstruction technique, as shown in Fig. 3. The updated inner-wall reflection positions also improved the consistency, eliminating band transition oscillations, and absolute profile positions, as seen in Fig. 10. In order to evaluate the absolute reflectometry profile positions after these major updates, the reflectometry pedestal position was benchmarked against the HRTS pedestal positions, see Fig. 11, using the methodology described in Sec. II.

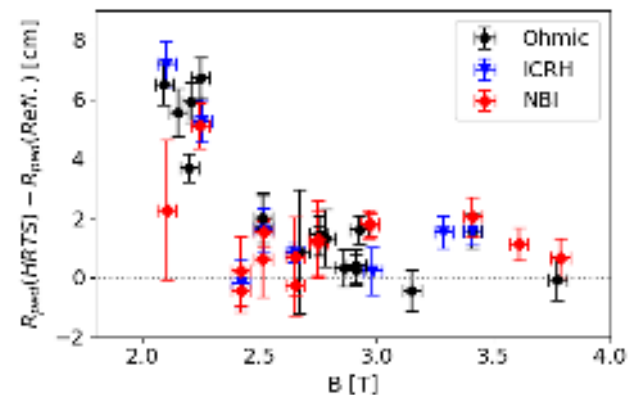


FIG. 11. Benchmark of reflectometry pedestal position in comparison to HRTS for several heating schemes applied and on-axis toroidal field. Pulses were randomly extracted from JET's C38 campaign while HRTS had a constant calibration applied. Only steady-state periods in the discharge corresponding to a high reflectometry acquisition rate were used, with each point in the plot corresponding to the average of ten consecutive HRTS triggers. For equivalent later comparison to the burst method using ten sweeps, the ten closest reflectometry profiles are averaged at each HRTS trigger.

Each point is the average of ten gap calculations from ten consecutive HRTS triggers during a steady-state plasma and high reflectometry sweep repetition. At each HRTS trigger, the HRTS profile is compared to the average of the eight closest reflectometry profiles. To identify any further discrepancy tendencies, the results display the corresponding heating scheme and are laid out as a function of the on-axis toroidal magnetic field to observe the isolated contribution of each

probing band. No clear trend is observed with respect to the plasma heating scheme applied, but a significant transition is observed when going below 2.4 T magnetic field on-axis. The overall agreement goes from 0.5cm +/-1.5cm to 5cm +/-2cm. This is the evidence of an additional discrepancy source at low magnetic field, which is the exact magnetic field range where the Q-band is used to probe the plasma edge. The next sections go over further overall improvements in absolute position and robustness, but specifically in Sec. VI, the improvements that are band-dependent and affect mostly the Q-band, thus eliminating this increased discrepancy at low magnetic field.

## VI. OPTIMIZED SWEEPING PARAMETERS AND VACUUM FIT

Upon investigating the sweeping parameters, it was found that the requested sweep-time parameter was being truncated before being passed to the controllers, and the value saved in the database for further processing was the truncated requested one and not the one set at the controller. The first issue with the truncation was easily solved by increasing the number of decimal places in the sweep-time parameter. The second issue, i.e. the parameter mismatch between the controller and database, happens because the controller coarsely interpolates the requests within a database of discrete values. For example, when requesting a sweep time of 11  $\mu s$ , the controller is actually set at 10.97  $\mu s$ . This mismatch was solved by starting to request values that the controller can set exactly, like the 10.97  $\mu s$ . The probing band most affected by both these issues was the Q-band, as it had by far the highest percentage mismatch in sweeping-time requested, 5.5  $\mu s$ , against the truncated and actually saved 6  $\mu s$ . A comparison of all sweep-time parameters loaded at the controller and their original requests and saved values is shown in Table I, and the same comparison for the updated parameters in Table II.

Band	Sweep-time requested	Loaded	Database
1 Q-IST	5.5 $\mu s$	5.53 $\mu s$	6 $\mu s$
2 V-IST	10 $\mu s$	10.01 $\mu s$	10 $\mu s$
3 W-IST	12 $\mu s$	12.01 $\mu s$	12 $\mu s$
4 V-CEA	10 $\mu s$	10.01 $\mu s$	10 $\mu s$
5 W-CEA	11 $\mu s$	10.97 $\mu s$	11 $\mu s$
6 D-CEA	11.5 $\mu s$	12.01 $\mu s$	12 $\mu s$

TABLE I. Original sweep-time parameters as requested on the second column, as loaded at the controllers on the third column, and as saved in the database for further processing on the fourth column.

An additional optimization implemented was the automatic narrow band-pass filtering of the vacuum pre-plasma measurement only allowing the echo from the inner wall to be left in the signal. This was again especially relevant for the Q-band since it operates at the waveguide's lower frequency limit and the signal amplitude compared to the background noise (signal-to-noise ratio) is not as good as for the other bands. Without the filtering, the fit in the vacuum group de-

Band	Sweep-time requested	Loaded	Database
1 Q-IST	5.53 $\mu s$	5.53 $\mu s$	5.53 $\mu s$
2 V-IST	10.01 $\mu s$	10.01 $\mu s$	10.01 $\mu s$
3 W-IST	12.01 $\mu s$	12.01 $\mu s$	12.01 $\mu s$
4 V-CEA	10.01 $\mu s$	10.01 $\mu s$	10.01 $\mu s$
5 W-CEA	10.97 $\mu s$	10.97 $\mu s$	10.97 $\mu s$
6 D-CEA	11.45 $\mu s$	11.45 $\mu s$	11.45 $\mu s$

TABLE II. Updated sweep-time parameters as requested on the second column, as loaded at the controllers on the third column, and as saved in the database for further processing on the fourth column.

lay is easily disturbed by the background noise and further emphasized whenever this band showed any degradation of signal quality - see an example in Fig. 12.

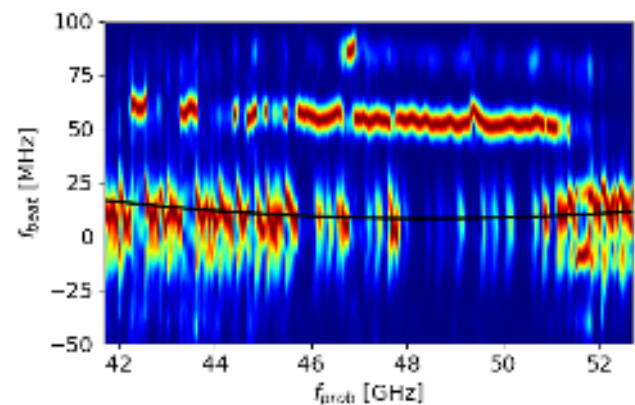


FIG. 12. Worst case scenario of  $f_{beat}$  (normalized at each  $f_{prob}$  slice) fitting without an optimized filter when the Q-band signal is faint and the noise level is high. The black line shows the spline fit obtained from fitting the maximums along the probing frequency. JET pulse 96201, 10 stacked sweeps of pre-plasma measurement.

Fig. 13 shows how the narrow band-pass filtering allows for an appropriate fitting of the beat frequency from the probing waves reflected at the inner-wall limiter. The band-pass filter can be optimized to be very narrow since it was verified that the waveguides dispersion is significantly stable even across different experimental campaigns several years apart. With the optimizations in this section in place, the agreement to HRTS for the low-field discharges matched that of the high-field discharges, as will be shown later, in Sec. X, with another benchmark also including the additional improvements in Secs. VII and VIII.

## VII. RIPPLE EFFECT IN THE MAGNETIC FIELD PROFILE

As already mentioned in Sec. I, errors in the input magnetic field profile in the initialization region shift the entire reconstructed profiles. Because the probing waves start being reflected very close to the vessel's outer wall, and the reflec-

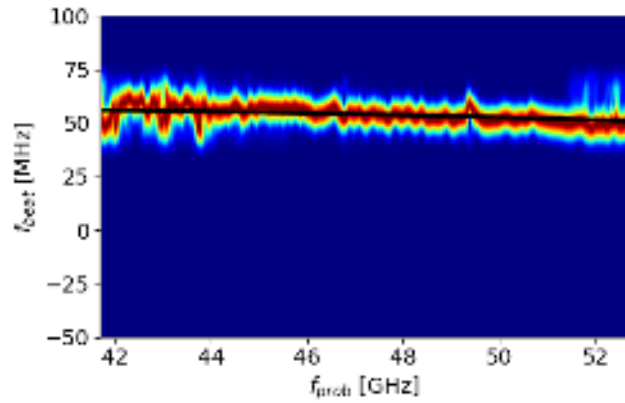


FIG. 13. Improved  $f_{beat}$  fitting result after a narrow band-pass filter (35 to 75 MHz) is applied in the same signal as Fig. 12. The black line shows the spline fit obtained from fitting the maximums along the probing frequency. JET pulse 96201, 10 stacked sweeps of pre-plasma measurement.

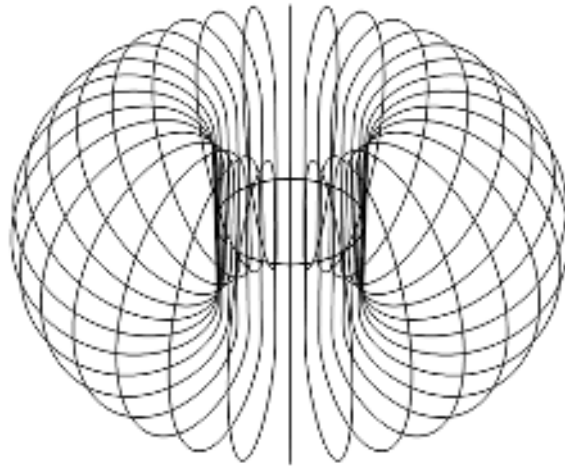


FIG. 14. 3D view of all toroidal field coils in JET, each represented by a single filament.

tometry waveguides are located exactly in between two TF (toroidal field) coils, the initial cut-off positions are pushed inwards (towards the plasma core) because at the reflection locations they experience a lower magnetic field than that extracted from the equilibrium reconstruction as the average field. This effect is referred to as the ripple effect and it's due to the toroidal discretization of the toroidal field coils. The magnitude of this ripple effect has been modeled by calculating the total toroidal field contribution from all toroidal field coils along the line-of-sight of the reflectometry diagnostic. An illustration showing all toroidal field coils is shown in Fig. 14, with each coil represented by a single filament.

Each toroidal field coil in JET is made of two sets of twelve turns, as can be seen from the poloidal view in Fig. 15. To mimic the volume occupied by the coil also in the toroidal direction, each turn was represented by fifteen filaments as

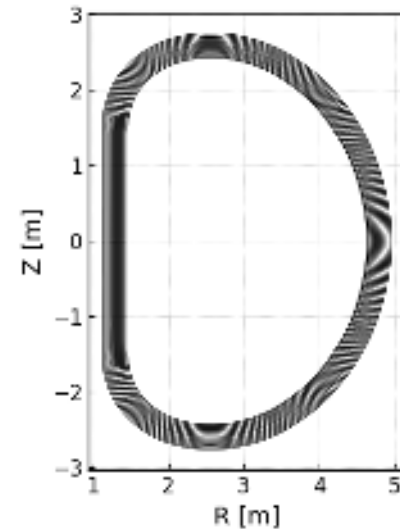


FIG. 15. Poloidal view of a toroidal field coil represented by two pancakes of 24 filaments.

shown in Fig. 16.

The resulting mismatch on the average toroidal field due to the ripple effect is displayed in Fig. 17. For the typical initialization positions between 3.85 and 4 m, the correction on the toroidal field is between 0.15 and 0.4%, respectively. An error of 0.4% in the estimated magnetic field when performing the initialization in JET typically results in an error introduced in the reconstructed profiles of  $\approx 0.7$  cm. Adding the ripple correction to the toroidal field makes the absolute position of the reflectometry profiles more consistent since the profiles with the outermost initialization position do not have an added discrepancy of up to 0.7 cm. Nonetheless, due to the magnitude of this change, it can't be experimentally validated against another measurement, e.g. from HRTS or interferometry, since the precision on HRTS positions, on the interferometry line-of-sight and the equilibrium and its line-of-sight mapping accuracy, are around a centimeter, see e.g. Fig 3.

### VIII. BURST MODE (GROUP DELAY FROM STACKED SPECTROGRAMS)

In theory, the profile reconstruction algorithm can use the instantaneous phase of the reflectometry signal and produce smooth monotonic density profiles with sub-millimeter accuracy<sup>6</sup>. In practice, due to the high level of turbulence in large-size tokamaks, there is often a high level of fluctuations in the density profiles that can cause spurious reflections, which in turn can cause a significant jitter in the reconstructed profiles. In JET discharges, this jitter can be over 10 cm at the worst-case scenarios (see example in Fig. 18) where the fluctuations also degrade the initialization technique, and typically of the order of 3 cm for the least affected pulses (see example in Fig. 19).

The two groups of jittering profiles in Fig. 18 show how using the phase from the instantaneous frequency can be dis-

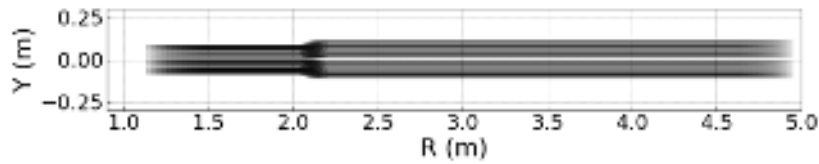


FIG. 16. Top view of a toroidal field coil with each turn represented by 15 filaments to mimic the toroidal volume.

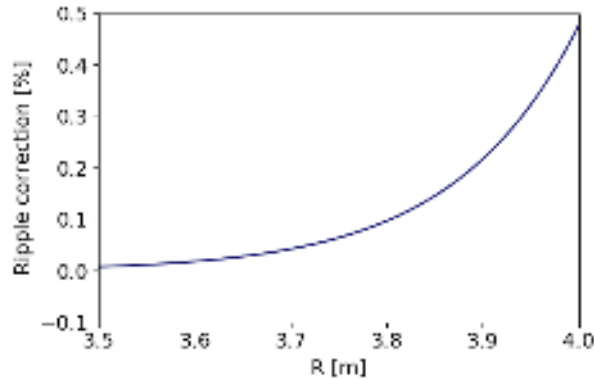


FIG. 17. Estimated ripple correction experienced by the reflectometry line-of-sight when approximating the toroidal field coils as a single filament.

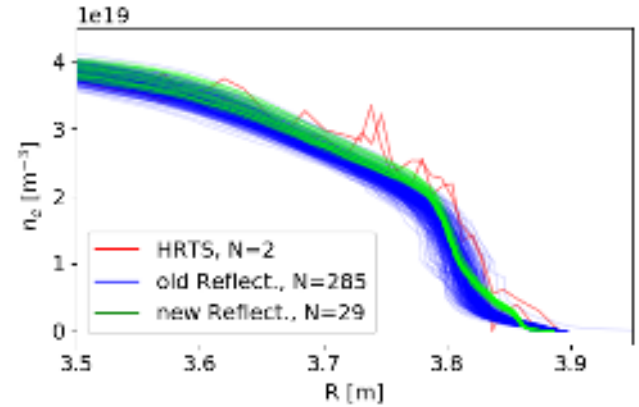


FIG. 19. Good case example comparing burst mode to instantaneous frequency input into profile reconstruction. JET pulse 93620, all profiles along 0.1s from  $t=7.8$ s, and stacked 10 sweeps in burst mode. N indicates the number of profiles plotted.

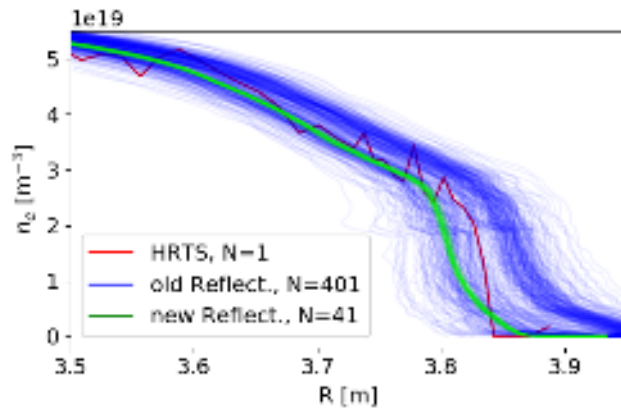


FIG. 18. Bad case example comparing burst mode to instantaneous frequency input into profile reconstruction. JET pulse 93898, all profiles along 0.05s from  $t=10$ s, and stacked 10 sweeps in burst mode. N indicates the number of profiles plotted.

turbed by additional echoes. In this specific case, there's an additional echo around the starting probing frequency  $f_{prob}^0$ . The echo can not only degrade the extraction of the phase increment data but also disturb the initialization algorithm to determine  $f_{prob}^0$ , and subsequently  $R_0$ , as explained by the definition of  $R_0$  in Eq. 3. The group delay data from the additional echo coupled with a lower starting probing frequency causes the jittering between the two clusters of reconstructed

profiles. With the burst mode, the determination of the starting frequency from the amplitude rise is more stable because the amplitude signal is an average of a burst of sweeps and the contribution of additional echoes is suppressed by emphasizing the maximum of the spectrogram following the reflection at the plasma cut-off. Even though it can be beneficial to the accuracy and robustness of the reconstructed profiles to stabilize the starting probing frequency, the main benefactor in this instance is the suppression of strong spurious reflections and additional echoes. This is demonstrated by Fig. 20, which shows the profiles reconstructed using the instantaneous frequency and the same starting probing frequency as determined by the amplitude rise from the burst of sweeps.

The burst analysis<sup>24</sup> is the best technique to suppress the spurious events by extracting the phase increment data, input data described by Eq. 2, from the integral of the group delay curve coming from the maximum of stacked beat-frequency spectrograms, following from Eq. 4. After implementing this technique in JET, the profile jitter is strongly suppressed to typically less than a centimeter as seen in Figs. 18 and 19, especially when stacking at least 4 frequency sweeps. Of course, stacking several frequency sweeps means integrating data over time, so one needs to bear in mind the averaging effect if the plasma changes within the integration time frame (which varies for different settings).

Apart from the necessary consideration of the integration time, the settings used to calculate the spectrograms also in-

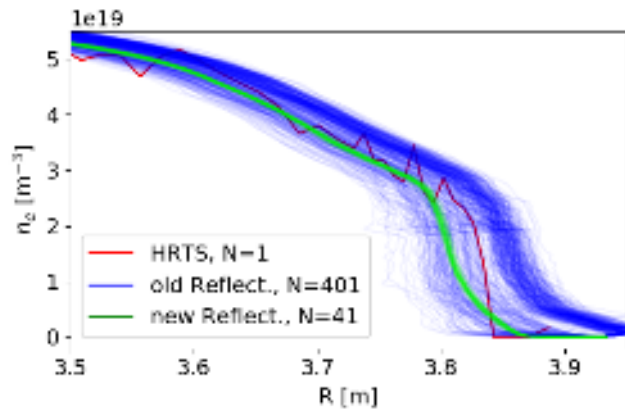


FIG. 20. Bad case example comparing burst mode to instantaneous frequency input into profile reconstruction. JET pulse 93898, all profiles along 0.05s from  $t=10$ s, and stacked 10 sweeps in burst mode.  $N$  indicates the number of profiles plotted. In this instance, the old reconstruction scheme with instantaneous frequency data was rerun with the same initialization choice as the burst algorithm.

fluence the extracted group delay and subsequently the reconstructed profile. Because the spectrogram is formed by several Fourier transforms, each point of the spectrogram maximum curve comes from the maximum of one Fourier transform that is calculated with a given window size. Increasing the window size means higher resolution in group delay, but since more points were used to calculate the Fourier transform, a lower time resolution is obtained (see example in Fig. 21). The opposite is true for shorter windows achieving higher time resolution, but lower group delay precision (see example in Fig. 22). These group delay plots are from synthetic data calculated with a full-wave 1D wave-equation code<sup>26,27</sup> (using a 4th order Runge-Kutta scheme<sup>28</sup>) and used as input profiles a common JET-like profile with pedestal and no added turbulence. The sweep rate and time resolution of the simulated signals match the experimental conditions in JET. The frequency band covered in Figs. 21 to 23 refers to a nearly continuous group delay along the steep pedestal and goes over the pedestal top when the group delay increases.

The three data types compared in Figs. 21 and 22 are the 1) spectrogram of reflectometry signal, extracted using the same technique as experimentally, i.e. an IQ demodulation of mixed detected and delayed injected signals; 2) a direct extraction of the phase from the reflectometry IQ signals, also known as instantaneous frequency; and 3) a signal calculated using the WKB approximation, i.e. the phase of each probing frequency is computed by integrating the refractive index along the probing wave path. The WKB signal is also shown because the reconstruction algorithm is based on the WKB approximation. This means that whenever the full-wave signal deviates from the WKB signal, the reconstruction algorithm will have errors in the calculation of the cut-off positions.

As seen in Figs. 21 and 22, different sections of the group delay data have different optimal window sizes. Shorter windows are needed to describe fast group delay changes, and

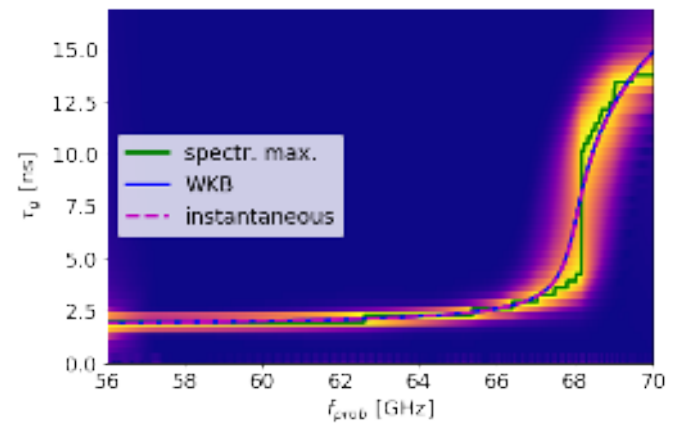


FIG. 21. Comparison between WKB, instantaneous group delay, and 256 points fixed-window spectrogram of synthetic reflectometry data from a JET-like plasma.

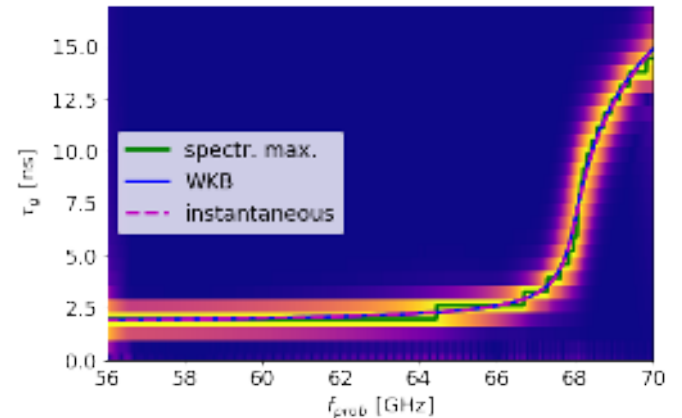


FIG. 22. Comparison between WKB, instantaneous group delay, and 128 points fixed-window spectrogram of synthetic reflectometry data from a JET-like plasma.

longer windows provide more accurate group delay data when it is not changing rapidly. The total profile error is somewhat proportional to the mismatch in the integral of the signal instead of the local mismatch magnitude since the recursive reconstruction algorithm adds the error cumulatively. To improve the extracted signal's accuracy, an algorithm was developed to minimize the dispersion at each  $f_{prob}$  channel in the spectrogram, equivalent to what is used in the burst analysis' original reference<sup>24</sup>, and initially introduced by D. Jones and R. Baraniuk<sup>29</sup>. An example of the spectrogram with adapted windows is shown in Fig. 23, with the red line being the window size at each step. Nevertheless, the adaptive spectrogram technique has settings that need to be tuned, i.e. how precise the method is in the presence of turbulence and how fast to transition between shorter and longer windows by tuning the minimization parameters. The complete optimization of these parameters and subsequent tests in more realistic data sets including turbulence is still underway and will be addressed in a future dedicated contribution specially focused on

the accuracy of the reconstructed profiles at the core plasma. This contribution focuses on the accuracy obtained on the absolute position of the reconstructed profiles (here observed as rigid shifts of the profile pedestal) and these are specifically affected by the precision of the profile reconstruction at the edge plasma. The probing of the edge plasma is typically observed in the reflectometer as a drop in group delay as the cut-off gradient increases. The faster the gradient increases, the steeper the decrease in group delay is. Optimizing the group delay extraction in this region is therefore critical to improve the absolute radial position. Fig. 24 shows a synthetic group delay signal for a turbulence-free JET-like plasma when the probing waves start to be reflected at the plasma cut-off and start dropping in group delay. For this typical steepness, Fig. 24 indicates that a window size as short as 25 is necessary to follow this fast-changing signal, which in this case agrees with the instantaneous frequency signal since no turbulence is present, and is therefore adopted to extract the group delay from the plasma edge.

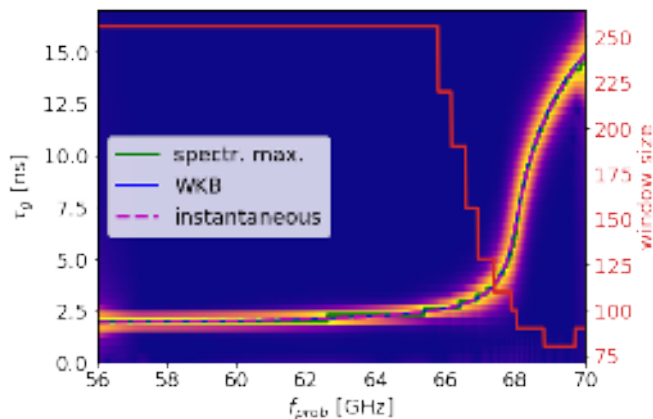


FIG. 23. Comparison between WKB, instantaneous group delay and adaptive spectrogram of synthetic reflectometry data from a JET-like plasma. The optimal window size is computed as in the burst analysis<sup>24,29</sup>.

## IX. PERSISTENT WRIGGLES

The use of the updated inner wall reflection positions and stacked spectrograms also revealed persistent profile oscillations (since the other oscillations were suppressed) coming from persistent oscillations in the reflectometry signal, mainly around 80 and 95 GHz. These are likely due to a non-linearity of the frequency sweep or the influence of secondary side lobes of the signal's spectrum. These oscillations are more evident when probing the plasma sharp pedestal due to the proximity to the waveguides and constant low group delay (in the order of 2 ns). See Fig. 25 for an example when these are clearly visible.

Since these fluctuations are persistent across pulses and campaigns, a compensation for them was computed by taking the average raw signal over several seconds minus a spline fit

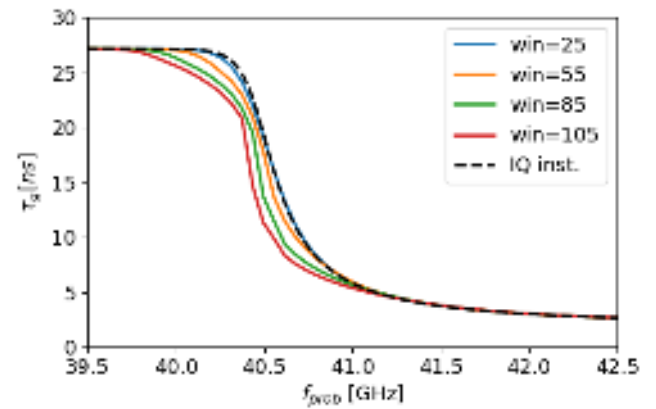


FIG. 24. Comparison between instantaneous group delay and scanning window sizes of the spectrogram of synthetic reflectometry data from a JET-like plasma. The signal corresponds to the first probing frequency band being reflected at the plasma cut-off.

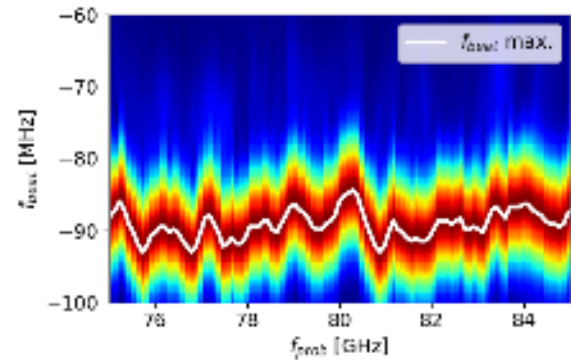


FIG. 25. Beat frequency example when the persistent fluctuations are present in a pedestal resulting in an approximately constant beat frequency. This example is present along the entire flat-top of JET pulse number 95272, from 11.5 to 23 s.

for the entire probing frequency band and the oscillations left can be later subtracted from the main signal. Fig. 26 shows the extracted group delay from the spectrogram maximum and spline fit for the example data in Fig. 25.

Implementing these wriggle corrections eliminated strong and unphysical localized profile oscillations. An example of affected profiles before applying this correction is given in Fig. 27, and when applied the correction, the resulting profiles are shown in Fig. 28.

Ideally, no fit or manipulation should be applied in the reflectometry signals since changing the total area under the group delay curve can affect the quality of the subsequent calculated cut-off positions due to the cumulative nature of the profile reconstruction algorithm. However, applying these corrections in the data analysis step is beneficial to the reconstructed profiles without showing any visible influence in the subsequent calculated cut-off positions as can be seen by comparing Fig. 27 to Fig. 28. A possible workaround in cases

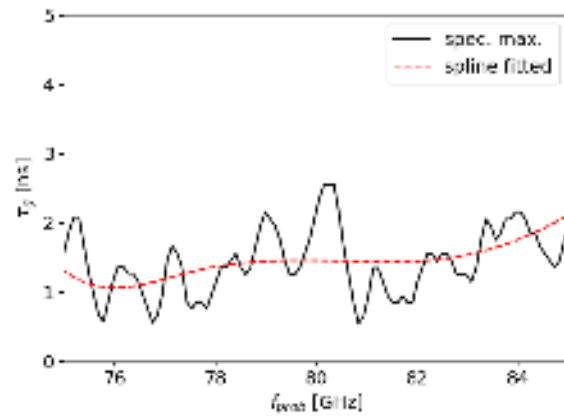


FIG. 26. Group delay extracted from the spectrogram maximum in Fig. 25 and a spline fit. The wriggle correction data is the difference between the two. Extracted from the flat-top of JET pulse number 95272.

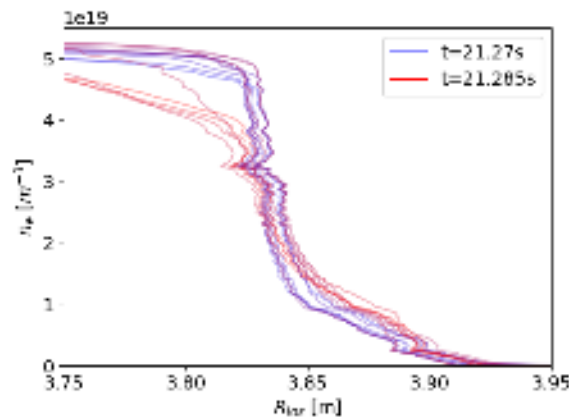


FIG. 27. Example of reconstructed density profiles strongly affected by the persistent beat frequency oscillations. JET pulse number 95272, with each profile color going gradually from blue at 21.27s, through purple and red at 21.285 s.

where shifts are introduced by such corrections would be to add the constraint on the spline fit to maintain the integral of the signal being corrected.

## X. TOTAL IMPROVEMENT IN ABSOLUTE PROFILE POSITION

Given all the introduced improvements in JET's profile reconstructions, another position benchmark was performed as shown in Fig. 29. The comparison spans over the on-axis total magnetic field again for a direct comparison to Fig. 11 and to highlight if any dependency is found on the frequency band probing the plasma. If any further benchmarks are done in further analysis, they could be compared against other experimental conditions to uncover specific physical drives that

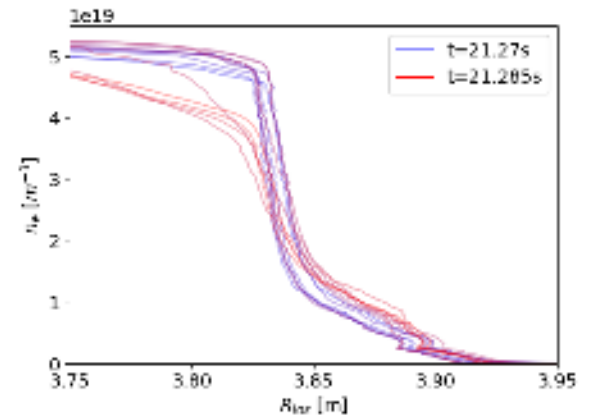


FIG. 28. Reconstructed electron density profiles of Fig. 27 after applying the wriggle correction computed from the data shown in Fig. 26. JET pulse number 95272, with each profile color going gradually from blue at 21.27 s, through purple and red at 21.285 s.

systematically move the absolute position of the reconstructed profiles.

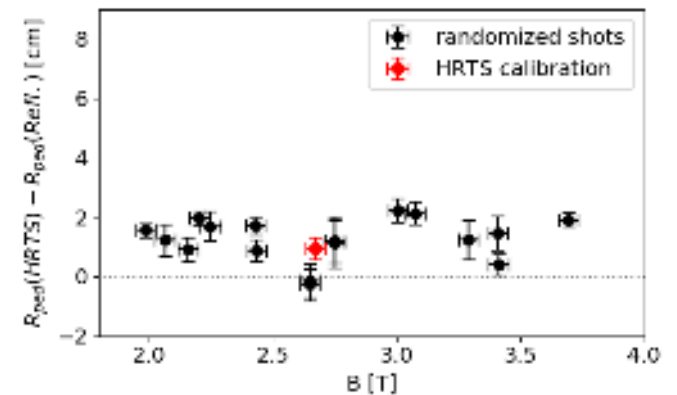


FIG. 29. Benchmark of reflectometry pedestal position in comparison to HRTS, using the same methodology as for Fig. 11, and explained in Sec. II. Pulses were randomly extracted from JET's C38 campaign with a mix of different heating schemes and while HRTS had a constant calibration applied. Only steady-state periods in the discharge corresponding to a high reflectometry acquisition rate were used, with each point in the plot corresponding to the average of ten consecutive HRTS triggers compared to the nearest reflectometry ten-stacked trigger.

Building from the first benchmark in Fig. 11, where it already included the upgraded equilibrium and updated inner-wall reflection positions, this benchmark additionally includes the ripple correction, updated sweep times, updated pre-plasma fitting, burst mode analysis, and wriggle corrections. The absolute position of reflectometry profiles is at this point mostly within zero and two centimeters (with a few barely exceeding points) when compared to the HRTS diagnostic in Fig. 29. The JET discharge 93477, highlighted with the red

symbol, is the HRTS position calibration shot for this pulse range. During the JET carbon wall period, the HRTS calibration used to match the position of a ruler bolted to the low-field-side wall. Once the metallic W-Be plasma facing components were installed and the ruler support was no longer available, the HRTS position calibration started to be performed against the reflectometry profiles using the same Ohmic discharge with a carbon wall reference and applying the same old toroidal field correction (around 0.5%) to force the reflectometer profiles to match the interferometry edge line-of-sight measurements.

Another element that has not yet been discussed is the starting density at the initialization of profile reconstruction. The typical assumption made at the initialization is that the starting density,  $n_{e0}$ , is null, such that the cut-off profile converges to the  $f_{ce}$  profile, and the starting position  $R_0$  is then found in the  $f_{ce}$  profile given by the equilibrium reconstruction. However, if the starting density is not null and assumed null, the cut-off profile does not completely converge to  $f_{ce}$  and the gap between the cut-off profile and  $f_{ce}$  at  $f_{prob}^0$  is introduced as an error in the determination of  $R_0$  in Eq. 3. If the starting density is known at the reconstruction initialization, the profile can be reconstructed without any significant detrimental effect on the profile accuracy, even if some shallow plasma has been skipped through<sup>10</sup>. Fig. 30 shows the position benchmark of Fig. 29 compared to it being recalculated with all initialization steps having a starting density of  $1.5 \times 10^{17} m^{-3}$ . It suggests that the remaining systematic discrepancy to HRTS can be at least in part due to a non-negligible starting density of around  $10^{17} m^{-3}$  for the reflectometry profiles to match the old HRTS position calibration using the in-vessel ruler. Unfortunately, the starting density in the initialization region can't be experimentally observed in JET but could be investigated in other set-ups and/or using an integrated inference scheme. The remaining one-centimeter oscillation is well within the experimental limits, especially since even the vessel coordinates have a one-centimeter accuracy and the equilibrium reconstruction also varies beyond one centimeter (see Fig. 3).

The burst mode and wriggle corrections (both from old band transitions and the corrected oscillations) also yield substantial improvements in profile stability and shape which aren't directly observed at the benchmark of absolute positions alone, except for the reduced error bars, which are already an obvious feature seen in Figs. 18 and 19.

The overall achieved improved stability and accuracy help significantly in subsequent data analyses due to the increased ability to track profile changes in much higher detail, e.g. to estimate particle losses due to ELMs<sup>30,31</sup> (demonstrated in the next section), to study transport<sup>31-34</sup>, to resolve tiny gas puff modulations generating density perturbations as small as one percent of the average density<sup>34-36</sup>, to characterize scrape-off layer plasmas for ICRF heating or detachment studies<sup>37,38</sup>, and to resolve in time fast profile changes due to the arrival of pacing pellets<sup>39,40</sup> or L-mode to H-mode transitions<sup>41,42</sup>.

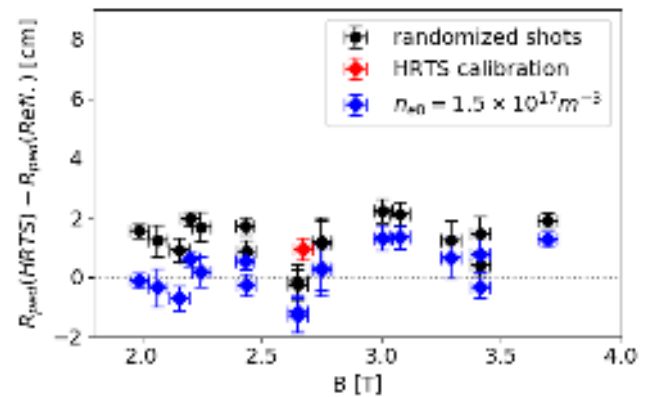


FIG. 30. Benchmark of reflectometry pedestal position in comparison to HRTS, using the same methodology as for Fig. 11, and explained in Sec. II. Pulses were randomly extracted from JET's C38 campaign with a mix of different heating schemes and while HRTS had a constant calibration applied. Only steady-state periods in the discharge corresponding to a high reflectometry acquisition rate were used, with each point in the plot corresponding to the average of ten consecutive HRTS triggers compared to the nearest reflectometry triggers. The blue diamond points used a non-zero starting density of  $1.5 \times 10^{17} m^{-3}$  at the initialization step.

## XI. EXAMPLE APPLICATION OF IMPROVED PROFILES TO ELM CYCLE

Beyond having profiles in a better radial position, the added robustness and better profile continuity allow to robustly track profile changes as can be observed in the case of the ELM cycles shown in Fig. 31.

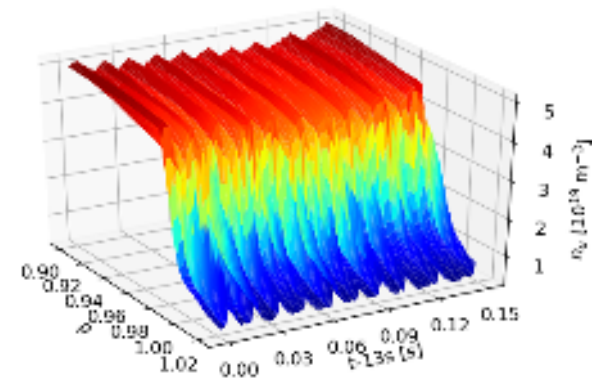


FIG. 31. Electron density profiles from JET pulse 96098 starting at 13s and showing ELM cycles of increased confinement and relaxation. Each density profile is reconstructed with all improvements described here and a burst of eight probing-frequency sweeps.

Several consecutive ELM cycles can be observed in Fig. 31, with a clear definition of the relaxation events increasing the edge density while simultaneously decreasing the core density. The obtained profiles follow the cycle quite robustly

with the use of all improvements described here and in this case, the profile reconstructions each used a stack of eight probing frequency sweeps. Even after the stacking and for a shot with settings optimized for a long high acquisition window, there's still enough temporal resolution to comfortably resolve the ELM cycles.

In order to observe the profile evolution in detail, all reconstructed profiles along the ten ELM cycles shown in Fig. 31 are overplotted in Fig. 32. The line color gradually goes from blue to red as the edge density increases. The high gradient pedestal and edge profiles are highly consistent, with the pedestal top having a higher variation of confined electrons. The resulting profile from the relaxation event is certainly linked to the starting profile and the starting core variation then carries out to a substantial variation in the maximum edge densities for different cycles.

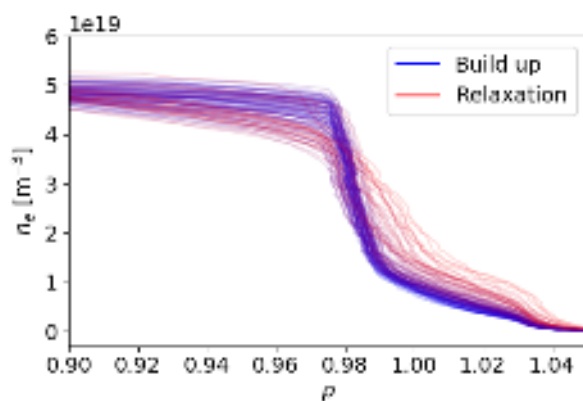


FIG. 32. Corresponding electron density profiles for ten ELM cycles in JET pulse 96098. The profile color gradually goes from blue at the lowest edge density (corresponding highest core density) to red at the highest relaxation with increased density outside the confined region ( $\rho > 1$ ). A total of 110 profiles are plotted, each reconstructed with a burst of eight probing-frequency sweeps.

In order to validate the observations from the reflectometry profiles, they can be compared to the interferometry edge line-of-sight measurements (LID4). Fig. 33 shows the comparison between the interferometry data and the reflectometry profiles integrated over the interferometry path, plus the total photon intensity from a visible spectroscopy measurement of the Be II line looking at the outer divertor. The intensity of Be II light sharply spikes exactly at the moment the ELMs crash in accordance with the reflectometry and interferometry data. The interferometry and reflectometry data are mostly in very good agreement both in crash timings and density values, which highlights the precision and robustness of the reconstructed reflectometry profiles.

## XII. CONCLUSIONS AND PROSPECTS

The limitations in benchmarking the absolute position of the reflectometry profiles to the HRTS profiles are manifold,

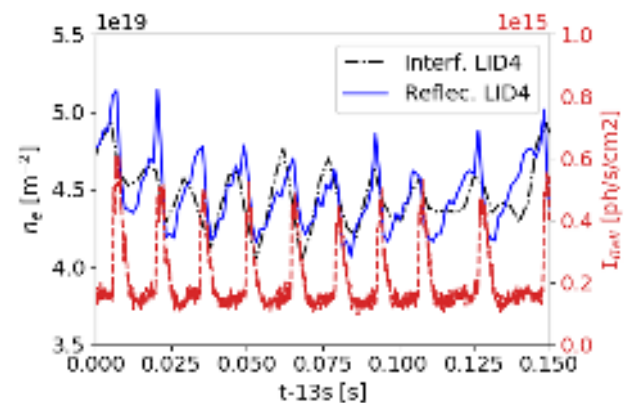


FIG. 33. Time traces of edge interferometry, reflectometry integrated over the interferometry line of sight, and total intensity of Be II emission looking at the outer divertor with the passive visible spectroscopy diagnostic. JET pulse 96098.

from the profile comparison technique to the precision of HRTS and the input equilibrium. Nevertheless, they serve as a good indication of the systematic absolute position of the reflectometry density profiles since systematic reflectometry position inaccuracies are mostly manifested as rigid shifts and because HRTS has very stable radial positions across a fixed calibration interval.

On the profile comparisons, the benchmarks done here use estimated pedestal positions with a simple yet robust technique. More sophisticated position comparisons can be done using fits on profiles but the parameter of interest focused on this work is the rigid radial shift, which is well observed by the methodology applied. A full comparison of profile accuracy would also take into account core and edge values, which is very impractical experimentally since the penetration of the probing waves from reflectometry is variable and the edge density estimated with other diagnostics has much larger uncertainties when compared to reflectometry.

The location of the HRTS profiles is calibrated against reflectometry profiles during a well-reproducible stable Ohmic discharge since the change of JET's carbon to Be-W plasma-facing components. Therefore, even though the same analysis is applied at each campaign calibration, the accuracy in the plasma reproducibility and equilibrium reconstruction used (not only to determine the background magnetic field but also for the mappings of different lines of sight) can affect the precision of this comparison. Ultimately, it's only natural that the accuracy of the reflectometry profiles cannot be better than that of the equilibrium reconstruction, since the X-mode reflectometry profiles are anchored at the plasma edge to the input magnetic field profile from the equilibrium.

Overall, several aspects of the profile reconstruction technique have been addressed here, from the input magnetic field, to updated inner-wall reflection positions, added an optimized ripple correction, optimized sweep time parameter and vacuum fits, and implemented the burst mode and wriggle corrections. All these combined significantly improved the stability

and accuracy of the absolute radial position of reconstructed reflectometry density profiles. There are no longer large unexpected profile movements linked to plasma current ramps, strong and persistent oscillations (zig-zags or wriggles) due to band transition or not, larger discrepancy in low magnetic field, and position jitters over several centimeters. They no longer require a correction in the input magnetic field and the pedestal position is now in  $1\pm 1$  cm agreement with the HRTS diagnostic, which is comparable to a similar agreement range between the equilibrium and HRTS in the C38 campaign and could also be systematically compensated by a starting initialization density of around  $1.5 \times 10^{17} m^{-3}$ , which dependency can be further investigated against different plasma parameters.

The ELM cycle example was shown to be easily observable with the reflectometry sweep repetition rate while maintaining good consistency automatically and in good agreement with the interferometry data. Due to the improved accuracy and robustness in JET's reflectometry density profiles, the reflectometry profiles have become more widely used by the fusion community, especially when a good description of the plasma edge and a higher temporal resolution are necessary, e.g. to estimate particle losses due to ELMs<sup>30,31</sup>, to study transport<sup>31–34</sup>, to resolve tiny gas puff modulations generating density perturbations as small as 1% of the average density<sup>34–36</sup>, to characterize scrape-off layer plasmas for ICRF heating or detachment studies<sup>37,38</sup>, and to resolve in time fast profile changes due to the arrival of pacing pellets<sup>39,40</sup> or L-mode to H-mode transitions<sup>41,42</sup>.

## ACKNOWLEDGMENTS

This work has been carried out within the framework of the EUROfusion Consortium, funded by the European Union via the Euratom Research and Training Programme (Grant Agreement No 101052200 — EUROfusion) and under the EUROfusion Enabling Research project ENRTEC.01.IST. Views and opinions expressed are however those of the author(s) only and do not necessarily reflect those of the European Union or the European Commission. Neither the European Union nor the European Commission can be held responsible for them.

This work has been part-funded by the EPSRC Energy Programme [grant number EP/W006839/1]. To obtain further information on the data and models underlying this paper please contact PublicationsManager@ukaea.uk.

## Appendix A: Validation of ray-tracing calculations

The ray-tracing calculations in Sec. IV are simple geometrical calculations since the condition in which the reference measurement is performed is before the plasma column is formed. Therefore, to validate the calculations, a simple comparison between the incident and exit rays is performed against the normal angles in the limiter and inner wall guard.

Fig. 34 shows a consistency between the incident and exit

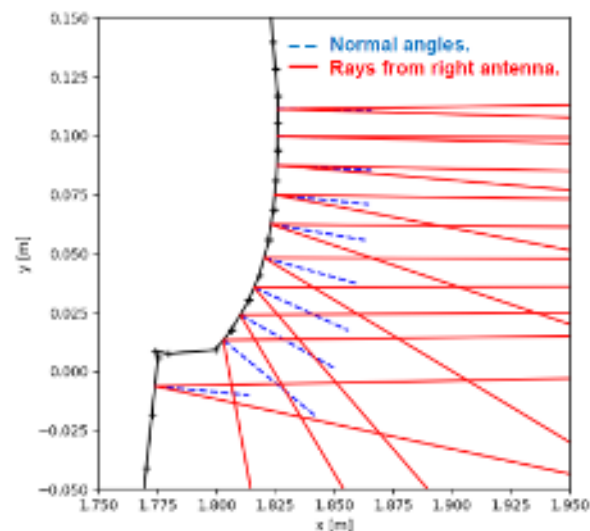


FIG. 34. Validation test of ray tracing calculations comparing incident and exit angles against the surface's normal angles. Calculated on a vacuum media since the reference measurement is performed before plasma breakdown.

angles with respect to the surface's normal, validating the calculations and results in Sec. IV.

## DATA AVAILABILITY

The data that support the findings of this study are available from the corresponding author upon reasonable request.

- <sup>1</sup>L. Meneses, L. Cupido, A. Sirinelli, M. E. Manso, and JET-EFDA Contributors, "First density profile measurements using frequency modulation of the continuous wave reflectometry on JET," *Review of Scientific Instruments* **79**, 10F108 (2008).
- <sup>2</sup>A. Sirinelli, B. Alper, C. Bottereau, F. Clairet, L. Cupido, J. Fessey, C. Hogben, L. Meneses, G. Sandford, M. J. Walsh, and JET-EFDA Contributors, "Multiband reflectometry system for density profile measurement with high temporal resolution on JET tokamak," *Review of Scientific Instruments* **81**, 10D939 (2010).
- <sup>3</sup>C. Bottereau, F. Clairet, J. Giacalone, D. Molina, R. Sabot, B. Alper, J. Fessey, A. Sirinelli, M. Walsh, L. Cupido, and L. Meneses, "Profile reflectometry upgrade on JET," *Proceedings of 9th International Reflectometry Workshop, IRW9, Lisbon*, <http://www.ipfn.ist.utl.pt/irw9/proceedings.html> (2009).
- <sup>4</sup>H. Bottollier-Curtet, *Réflexométrie hyperfréquence pour la détermination de la densité électronique et de ses fluctuations sur le tokamak Petula-B*, Ph.D. thesis, Université de Paris XI (1986).
- <sup>5</sup>D. A. Shelukhin, V. A. Vershkov, D. V. Sarychev, A. A. Petrov, V. G. Petrov, and G. F. Subbotin, "X-mode lower cutoff high field side reflectometer for electron density profile measurements in T-10 tokamak," *Proceedings of 11th International Reflectometry Workshop, IRW11, Palaiseau* (2013).
- <sup>6</sup>R. B. Morales, S. Hacquin, S. Heuraux, and R. Sabot, "New density profile reconstruction methods in X-mode reflectometry," *Review of Scientific Instruments* **88**, 043503 (2017).
- <sup>7</sup>S. Heuraux, F. Clairet, and F. D. Silva, "An X-mode reflectometry study on the reflection point for the density profile reconstruction," (2009).
- <sup>8</sup>C. Laviron, A. J. H. Donné, M. E. Manso, and J. Sanchez, "Reflectometry techniques for density profile measurements on fusion plasmas," *Plasma Physics and Controlled Fusion* **38**, 905 (1996).
- <sup>9</sup>E. Mazzucato, "Microwave reflectometry for magnetically confined plasmas," *Review of Scientific Instruments* **69**, 2201–2217 (1998).

- <sup>10</sup>R. B. Morales, *Density profile reconstruction methods for extraordinary mode reflectometry*, Ph.D. thesis, Université de Lorraine (2018).
- <sup>11</sup>J.-M. Moret, B. Duval, H. Le, S. Coda, F. Felici, and H. Reimerdes, "Tokamak equilibrium reconstruction code LIUQE and its real time implementation," *Fusion Engineering and Design* **91**, 1–15 (2015).
- <sup>12</sup>P. M. Carthy, L. Giannone, M. Dunne, R. Fischer, J. Fuchs, K.-H. Schubeck, ASDEX Upgrade Team, and EUROfusion MST1 Team, "Time-dependent ELM-resolved equilibrium reconstruction on ASDEX Upgrade," *Proceedings of the 22nd IAEA Fusion Energy Conference, Geneva* (2008).
- <sup>13</sup>G. Szepesi, L. C. Appel, E. de la Luna, L. Frassinetti, P. Gaudio, M. Gelfusa, S. Gerasimov, N. C. Hawkes, M. Sertoli, D. Terranova, and JET Contributors, "Advanced equilibrium reconstruction for JET with EFIT++," *Proceedings of the 47th EPS Conference on Plasma Physics, Sitges* (2021).
- <sup>14</sup>T. Fukuda, K. Nagashima, S. Konoshima, K. Haraguchi, T. Takahashi, A. Nagashima, and T. Matoba, "Broadband reflectometry for the density profile and fluctuation measurements in the JT-60 tokamak," *Review of Scientific Instruments* **61**, 3524–3527 (1990).
- <sup>15</sup>Z. Shoubiao, G. Xiang, L. Bili, W. Yumin, Z. Tao, H. Xiang, L. Zixi, B. Jingliang, and L. Jiangang, "Density profile and fluctuation measurements by microwave reflectometry on EAST," *Plasma Science and Technology* **16**, 311 (2014).
- <sup>16</sup>M. Hirsch, H. Hartfuss, T. Geist, and E. de la Luna, "Amplitude modulated heterodyne reflectometer for density profile and density fluctuation profile measurements at W7-AS," *Review of Scientific Instruments* **67**, 1807–1813 (1996).
- <sup>17</sup>P. Moreau, F. Clairet, J. M. Chareau, M. Paume, and C. Laviron, "Ultrafast frequency sweep heterodyne reflectometer on the Tore Supra tokamak," *Review of Scientific Instruments* **71**, 74–81 (2000).
- <sup>18</sup>F. Clairet, B. Ricaud, F. Briolle, S. Heurax, and C. Bottereau, "New signal processing technique for density profile reconstruction using reflectometry," *Review of Scientific Instruments* **82**, 083502 (2011).
- <sup>19</sup>L. Zeng, G. Wang, E. Doyle, T. Rhodes, W. Peebles, and Q. Peng, "Fast automated analysis of high-resolution reflectometer density profiles on DIII-D," *Nuclear Fusion* **46**, S677 (2006).
- <sup>20</sup>K. W. Kim, E. J. Doyle, W. A. Peebles, A. Ejiri, J. Luhmann, N. C., and C. L. Rettig, "Advances in reflectometric density profile measurements on the DIII-D tokamak," *Review of Scientific Instruments* **66**, 1229–1232 (1995).
- <sup>21</sup>K. W. Kim, E. J. Doyle, T. L. Rhodes, W. A. Peebles, C. L. Rettig, and N. C. Luhmann, Jr., "Development of a fast solid-state high-resolution density profile reflectometer system on the DIII-D tokamak," *Review of Scientific Instruments* **68**, 466–469 (1997).
- <sup>22</sup>N. A. Uckan, T. Uckan, and J. R. Moore, "Calculation of magnetic field ripple effects in circular and noncircular tokamaks," Master thesis, Oak Ridge National Laboratory (1976).
- <sup>23</sup>G. Saibene, R. Sartori, D. McDonald, M. Beurskens, A. Salmi, J. Lönnroth, V. Parail, P. de Vries, Y. Andrew, R. Budny, A. Boboc, I. Coffey, E. de la Luna, A. Loarte, P. Lomas, S. Gerasimov, C. Giroud, J. Hobirk, S. Hotchin, T. Johnson, C. Lescure, I. Nunes, N. Oyama, V. Riccardo, H. Urano, and JET EFDA contributors, "Gas scan to probe fuelling through the H-mode pedestal in JET," *Proceedings of the 22nd IAEA Fusion Energy Conference, Geneva* (2008).
- <sup>24</sup>P. Varela, M. Manso, A. Silva, the CFN Team, and the ASDEX Upgrade Team, "Review of data processing techniques for density profile evaluation from broadband FM-CW reflectometry on ASDEX Upgrade," *Nuclear Fusion* **46**, S693 (2006).
- <sup>25</sup>J. Simpson, D. Moulton, C. Giroud, M. Groth, and G. Corrigan, "Using EDGE2D-EIRENE to simulate the effect of impurity seeding and fuelling on the upstream electron separatrix temperature," *Nuclear Materials and Energy* **20** (2019).
- <sup>26</sup>M. Colin, *Modelisations d'un reflectometre mode X en vue de caracteriser les fluctuations de densite et de champ magnetique: Applications aux signaux de Tore Supra*, Ph.D. thesis, Université de Lorraine (2001).
- <sup>27</sup>S. Heurax and F. da Silva, "Simulations on wave propagation in fluctuating fusion plasmas for reflectometry applications and new developments," *Aims Journal Discrete and Continuous Dynamical Systems - Series S DCDS-S 5*, 307–328 (2012).
- <sup>28</sup>W. H. Press, B. P. Flannery, S. A. Teukolsky, and W. T. Vetterling, *Runge-Kutta Method, §16.1 in Numerical Recipes in FORTRAN: The Art of Scientific Computing, 2nd ed.* (Cambridge University Press, 1992) pp. 704–716.
- <sup>29</sup>D. Jones and R. Baraniuk, "A simple scheme for adapting time-frequency representations," *IEEE Transactions on Signal Processing* **42**, 3530–3535 (1994).
- <sup>30</sup>L. Horvath, B. Lomanowski, J. Karhunen, M. Maslov, P. A. Schneider, J. Simpson, M. Brix, B. Chapman-Oplopoiou, G. Corrigan, L. Frassinetti, M. Groth, K. Lawson, C. F. Maggi, S. Menmuir, R. B. Morales, D. Moulton, O. Myatra, D. Nina, T. Pereira, D. I. Réfy, S. Saarelma, M. Vécsei, and JET Contributors, "Pedestal particle balance studies in JET-ILW H-mode plasmas," *Plasma Physics and Controlled Fusion* **65**, 044003 (2023).
- <sup>31</sup>L. Frassinetti, C. P. von Thun, B. Chapman-Oplopoiou, H. Nyström, M. Poradzinski, J. Hillesheim, L. Horvath, C. Maggi, S. Saarelma, A. Stagni, G. Szepesi, A. Bleasdale, A. Chomiczewska, R. Morales, M. Brix, P. Carvalho, D. Dunai, A. Field, J. Fontdecaba, H. Sun, D. King, D. Kos, E. Kowalska, B. Labit, M. Lennholm, S. Menmuir, E. Rachlew, D. Refy, P. Schneider, E. Solano, N. Vianello, M. Vécsei, and JET Contributors, "Effect of the isotope mass on pedestal structure, transport and stability in D, D/T and T plasmas at similar  $\beta_N$  and gas rate in JET-ILW type I ELMy H-modes," *Nuclear Fusion* **63**, 112009 (2023).
- <sup>32</sup>T. Tala, A. Mariani, A. Salmi, E. R. Solano, I. S. Carvalho, A. Chomiczewska, E. Delabie, F. Eriksson, J. Ferreira, E. Fransson, L. Horvath, P. Jacquet, D. King, A. Kirjasuo, S. Leerink, E. Lerche, C. Maggi, P. Mantica, M. Marin, M. Maslov, S. Menmuir, R. B. Morales, V. Naulin, M. F. F. Nave, H. Nordman, C. P. V. Thun, P. A. Schneider, M. Sertoli, and K. Tanaka, "Comparison of particle transport and confinement properties between the ICRH and NBI heated dimensionless identity plasmas on JET," *Proceedings of the 47th EPS Conference on Plasma Physics, Sitges* (2021).
- <sup>33</sup>T. Tala, F. Eriksson, P. Mantica, A. Mariani, A. Salmi, E. R. Solano, I. Carvalho, A. Chomiczewska, E. Delabie, J. Ferreira, E. Fransson, L. Horvath, P. Jacquet, D. King, A. Kirjasuo, S. Leerink, E. Lerche, C. Maggi, M. Marin, M. Maslov, S. Menmuir, R. B. Morales, V. Naulin, F. Nave, H. Nordman, C. P. von Thun, P. A. Schneider, M. Sertoli, and K. Tanaka, "Role of NBI fuelling in contributing to density peaking between the ICRH and NBI identity plasmas on JET," *Nuclear Fusion* **62**, 066008 (2022).
- <sup>34</sup>T. Tala, A. Järvinen, C. Maggi, P. Mantica, A. Mariani, A. Salmi, I. Carvalho, A. Chomiczewska, E. Delabie, F. Devasagayam, J. Ferreira, W. Gromelski, N. Hawkes, L. Horvath, J. Karhunen, D. King, A. Kirjasuo, E. Kowalska-Strzeciwiłk, S. Leerink, M. Lennholm, B. Lomanowski, M. Maslov, S. Menmuir, R. B. Morales, R. Sharma, H. Sun, K. Tanaka, and JET Contributors, "Isotope mass scaling and transport comparison between JET deuterium and tritium L-mode plasmas," *Nuclear Fusion* **63**, 112012 (2023).
- <sup>35</sup>A. Salmi, D. King, J. Karhunen, S. Mordijck, R. B. Morales, V. Naulin, and JET Contributors, "Gas scan to probe fuelling through the H-mode pedestal in JET," *Proceedings of the 47th EPS Conference on Plasma Physics, Sitges* (2021).
- <sup>36</sup>A. Salmi, T. Tala, R. B. Morales, I. Carvalho, and P. J. Lomas, "Electron density pedestal behaviour in strike-point sweeping experiment on JET," *Plasma Physics and Controlled Fusion* **65**, 055025 (2023).
- <sup>37</sup>M. J. Mantsinen, P. Jacquet, E. Lerche, D. Gallart, K. Kirov, P. Mantica, D. Taylor, D. V. Eester, M. Baruzzo, I. Carvalho, C. D. Challis, A. D. Molin, E. Delabie, E. de la Luna, R. Dumont, P. Dumortier, J. Eriksson, D. Frigione, J. Garcia, L. Garzotti, C. Giroud, R. Henriques, J. Hobirk, A. Kappatou, Y. Kazakov, D. Keeling, D. King, V. Kiptily, M. Lennholm, P. Lomas, C. Lowry, C. Maggi, J. Mailloux, M. Maslov, S. Menmuir, I. Monakhov, R. B. Morales, C. Noble, M. Nocente, A. Patel, G. Pucella, C. Reux, D. Rigamonti, F. Rimini, A. Sheikh, S. Silburn, P. Siren, E. R. Solano, Z. Stancar, M. Tardocchi, and JET Contributors, "Experiments in high-performance JET plasmas in preparation of second harmonic ICRF heating of tritium in ITER," *Nuclear Fusion* **63**, 112015 (2023).
- <sup>38</sup>M. Groth, S. Aleiferis, S. Brezinsek, M. Brix, I. Carvalho, P. Carvalho, N. Horsten, I. Jepu, J. Karhunen, K. Kirov, H. Kumpulainen, B. Lomanowski, K. Lawson, C. Lowry, A. Meigs, S. Menmuir, R. B. Morales, E. Pawelec, T. Pereira, A. Shaw, S. Silburn, B. Thomas, V. Solokha, S. Wiesen, D. Borodin, P. Beaumont, J. Bernardo, I. Coffey, N. Conway, E. de la Luna, D. Douai, D. Dunai, C. Giroud, R. Gomes, J. Hillesheim, L. Horvath, A. Huber, S. Jachmich, P. Lomas, C. Maggi, M. Maslov, C. P. von Thun, G. Petravich, D. Refy, S. Scully, G. Sergienko, Z. Stancar, N. Vianello, B. Viola, M. Wischmeier, and the JET Contributors, "Characterisation of the SOL conditions and detachment in JET-ILW hydrogen,

This is the author's peer reviewed, accepted manuscript. However, the online version of record will be different from this version once it has been copyedited and typeset.  
PLEASE CITE THIS ARTICLE AS DOI: 10.1063/5.0176696

deuterium and tritium low-confinement mode plasmas," submitted to Nuclear Fusion (2024).

- <sup>39</sup>M. Valovic, P. Blatchford, A. Boboc, M. Brix, I. Carvalho, P. Carvalho, J. M. Fontdecaba Climent, L. Frassinetti, L. Garzotti, F. Koechl, C. Lowry, E. de la Luna, C. Maggi, R. B. Morales, S. Nowak, F. Rimini, S. Silburn, G. Tvalashvili, Štancar, S. Aleiferis, D. Dunai, D. Refy, M. Vecsei, C. Olde, and JET Contributors, "Control of plasma density and isotope mix by peripheral fuelling pellets in JET D-T experiments," submitted to Nuclear Fusion (2024).
- <sup>40</sup>L. Garzotti, D. Frigione, P. Lomas, F. Rimini, D. Van Eester, S. Aleiferis, E. Alessi, F. Auriemma, R. B. Morales, I. Carvalho, P. S Carvalho, A. Chomiczewska, E. De La Luna, R. Ferreira, A. Field, M. Fontana, L. Frassinetti, S. Gabriellini, W. Gromelski, I. Ivanova-Stanik, V. Kiptili, M. Kirov, K andLennholm, C. Lowry, C. Maggi, J. Mailloux, S. Menmuir, S andNowak, V. Parail, A. Pau, C. Perez von Thun, L. Piron, G. Pucella, C. Reux, O. Sauter, C. Sozzi, Z. Stancar, C. Stuart, H. Sun, G. Telesca, D. Tskakaja, M. Valovic, N. Wendler, V. K. Zotta, and JET Contributors, "Development of high current baseline scenario for high deuterium-tritium fusion performance at JET," submitted to Nuclear Fusion (2024).
- <sup>41</sup>C. Silva, E. Solano, J. Hillesheim, E. Delabie, G. Birkenmeier, L. Gil, C. Giroud, R. B. Morales, D. Nina, and JET Contributors, "Effect of the

divertor configuration on the JET edge radial electric field," Nuclear Fusion **62**, 126057 (2022).

- <sup>42</sup>E. Solano, G. Birkenmeier, C. Silva, E. Delabie, J. Hillesheim, A. Baciero, I. Balboa, M. Baruzzo, A. Boboc, M. Brix, J. Bernardo, C. Bourdelle, I. Carvalho, P. Carvalho, C. Challis, M. Chernyshova, A. Chomiczewska, R. Coelho, I. Coffey, T. Craciunescu, E. de la Cal, E. de la Luna, R. Dumont, P. Dumortier, M. Fontana, J. Fontdecaba, L. Frassinetti, D. Gallart, J. Garcia, C. Giroud, W. Gromelski, R. Henriques, J. Hall, A. Ho, L. D. Horton, L. Horvath, P. Jacquet, I. Jepu, E. Joffrin, A. Kappatou, D. Kos, P. Lomas, D. Keeling, D. King, E. Kowalska-Strzęciwilk, M. Lennholm, E. Lerche, E. Litherland-Smith, V. Kiptily, K. Kirov, A. Loarte, B. Lomanowski, C. Maggi, J. Mailloux, M. Mantsinen, M. Maslov, A. Meigs, I. Monakhov, R. B. Morales, A. Nielsen, D. Nina, C. Noble, E. Pawelec, M. Poradzinski, G. Pucella, P. Puglia, D. Réfy, J. Rasmussen, E. Righi, F. Rimini, T. Robinson, M. Sertoli, S. Silburn, G. Sips, P. Sirén, Štancar, H. Sun, G. Szepesi, D. Taylor, B. Thomas, E. Tholerus, G. Verdoolaeye, P. Vincenzi, B. Viola, N. Vianello, T. Wilson, and JET Contributors, "L-H transition studies in Tritium and Deuterium-Tritium campaigns at JET with Be wall and W divertor," Nuclear Fusion **63**, 112011 (2023).